Solar Energy Materials & Solar Cells 254 (2023) 112247

Contents lists available at ScienceDirect

Solar Energy Materials and Solar Cells

journal homepage: www.elsevier.com/locate/solmat

Manganese-substituted kesterite thin-films for earth-abundant photovoltaic applications

Vanira Trifiletti [a], Luigi Frioni [a,b], Giorgio Tseberlidis [a], Elisa Vitiello [a], Mati Danilson [c], Maarja Grossberg [c], Maurizio Acciarri [a], Simona Binetti [a,*], Stefano Marchionna [b]

[a] Department of Materials Science and Solar Energy Research Center (MIB-SOLAR), University of Milano-Bicocca, Via Cozzi 55, I-20125, Milan, Italy
[b] Ricerca sul Sistema Energetico - RSE S.p.A., Via R. Rubattino 54, 20134, Milan, Italy
[c] Department of Materials and Environmental Technology, Tallinn University of Technology, Ehitajate tee 5, 19086, Tallinn, Estonia

ARTICLE INFO

Keywords:
Manganese
Solar cell
Secondary phase
Defect states
Post-deposition treatment
Ageing effect

ABSTRACT

Thin film photovoltaic devices based on CdTe and $Cu(In,Ga)Se_2$ find in $Cu_2ZnSn(S,Se)_4$-based technology a more eco-friendly alternative. To further reduce production costs and improve sustainability, other abundant metals, such as manganese, can be tested as a potential alternative to zinc. Mn is a safe and Earth-abundant element, and it can be used in light absorber materials when it is part of quaternary chalcogenides with copper and tin. This work reports on the growth and characterization of Cu_2MnSnS_4 thin films produced by a two-step deposition process. The metallic precursors have been deposited by sputtering and the stack annealed at high temperatures in sulphur atmosphere. The layers, obtained in Cu-poor Mn-poor compositional regime, have been tested in solar devices with a record efficiency of 1.13% and a high open-circuit voltage of about 445 mV delivered by the champion device after over one year from the first PV measurement. X-ray diffraction and X-ray photoelectron, Raman, photoluminescence, and admittance spectroscopies have been used to investigate the Cu_2MnSnS_4 defectivity, and a scenario of high defects has emerged. Therefore, to promote the development of Mn-based photovoltaics the synthesis methodology should be optimized and the device architecture should be specifically designed for the compound.

1. Introduction

Thin film (TF) photovoltaic (PV) devices are a powerful way to further reduce the levelized cost of energy, which is a measure of the electricity production cost for a power plant over its lifetime. Therefore, PV should guarantee both affordable production costs and high efficiency for many years [1]. Regarding thin-film (TF) technologies, the best results have been obtained with CdTe and $Cu_2InGaSe_4$ (CIGS) solar cells which reached record efficiencies of 22.1% and 23.4%, respectively [2]. PV modules based on these chalcogenides are already available on the market with good performance [3,4]: CdTe and CIGS modules approach the 20% efficiency, but one of the main constraint factors to their mass-scale production is the use of rare elements, classified as critical raw materials [1]. Despite the remarkable efficiencies of the TF-PV technologies and the successful application in flexible PV devices [5], the need of handling eco-friendly and cheap compounds has constantly pushed the research toward more environmental friendly materials, such as $Cu_2ZnSn(S,Se)_4$ (CZTSSe) [6–9]. Close to 13% [2], the current record efficiency for CZTSSe solar cells highlights the strong potentialities of this abundant chalcogenide to support a sustainable energy transition. Recently, another compound has been put under the spotlight: $Cu_2MnSn(S,Se)_4$ (CMTSSe) with a record efficiency of about 1.8% [10–12]. Manganese is more abundant than Zinc (1100 ppm against 79 ppm) [7,13], leading to a potentially cheaper final device. The application of Mn-substituted CZTSSe in solar cells has been predicted to be able to reach efficiencies up to 6.9% with an Mn content between 10% and 20% [14]. To furtherly improve the global sustainability of this kind of TF-PV device, the selenium content should be reduced or erased, being a rare and toxic element [15]. Actually, Pansuriya recently calculated that the pure sulphide CMTS could reach about 20.3% efficiency in dedicated device architecture [16]. The authors highlight that the substitution of the CdS buffer layer is crucial for increasing the CMTS PV efficiency: the calculated value was reached by simulating the use of SnS as a buffer layer [16]. CMTS has an optical band gap (E_g) in the range of 1.2–1.6eV, suitable for PV applications, and an absorption coefficient higher than 10^4 cm^{-1}. It can be

* Corresponding author.
E-mail address: simona.binetti@unimib.it (S. Binetti).

https://doi.org/10.1016/j.solmat.2023.112247
Received 28 July 2022; Received in revised form 16 January 2023; Accepted 14 February 2023
Available online 22 February 2023

synthesised using various deposition methods: solvothermal methodologies [17–19], hot injection [20,21], spin coating [14,22,23], sol-gel synthesis [24–26], single-crystal chemical transport reaction [27], dip-coating [28,29], spray pyrolysis [30–33], thermal evaporation [34], co-sputtering [35], electrodeposition [36,37] and hydrothermal synthesis [38,39]. Nevertheless, the research on pure-sulphide CMTS is still in its infancy. Further fundamental studies should be carried out to better correlate the PV performances with the stoichiometry, the secondary phase formation, the crystal growth, and the band alignment with the other layers making up the PV device. The maximum PV efficiency reached by a CMTS/CdS solar cell was of 0.83% with open-circuit voltage (V_{oc}) of 354 mV, and it was synthesised through thermal evaporation of the metal precursors, followed by a sulfurization process in argon atmosphere with elemental sulphur [40].

In this work, we propose the CMTS TF growth by the deposition of the metallic precursors via the sputtering technique, followed by sulfurization at high temperatures. The sputter deposition has been selected to explore the usage of a methodology able to guarantee at the same time a good control of growth parameters and an easy scale-up at the industrial level. A few years ago, the same method has been positively tested to deposit CZTS TFs with preliminary solar cells efficiency of up to 4%; the best PV results have been measured on samples obtained by the sulfurization at 570 °C of a metallic precursors stack deposited by DC sputtering [41]. The sputtering versatility allowed the growth of CMTS TFs controlling the ratio of the metals and overcome the Mn sublimation occurring by using the thermal evaporation technique, ahich hinder the control of the deposition flux. The aim of this work is to investigate the correlation between composition, chemical-physic properties, and PV performances. The maximum efficiency achieved was initially 0.65%, but in just over a year it almost doubled. Although the recording device has achieved a PV efficiency of 1.13%, this value is extremely far from the predicted 20% [16]. The reasons for the low efficiencies have been researched, the detrimental defects identified, and a way-out strategy suggested.

2. Material and methods

The CMTS absorber layer has been deposited on a soda-lime glass (SLG) substrate (area: 3 × 2.5 cm^2) with and without molybdenum-coating (800 nm) as the back contact of the final PV device. Samples on SLG have been used to carry out UV/Visible absorption spectroscopy measurements, which have been performed to estimate the CMTS TFs optical bandgap, E_g, via Tauc plot [42]. A confocal sputtering system (Kenosistec KS 300C) with 3 magnetron sources (5 cm target diameter) has been used to deposit the metallic precursors' stack. Cu, Sn and Mn high purity target (99.99% Kurt J. Lesker) has been employed as metallic sources, and the value of 6 × 10^{-3} has been used as argon partial pressure during the whole deposition process. Also, the metal sequence in the stack has been set for all the CMTS samples as follows: Sn/Cu/Mn. The deposition order has been selected to minimize the tin loss during the sulfurization process, induced by the high volatility of its sulphides [9,41]. DC sputtering deposition power was settled at 20 W, 80 W and 45 W respectively for Sn (to avoid melting), Cu and Mn (to avoid cracking). In the first series, the deposition time has been tuned to obtain CMTS TFs in the desired compositional range. In the case of the Mn tuning samples' set, the deposition time was 1450 s for Sn, 510 s for Cu, and Mn is tuned (Mn-rich for 1400 s, Mn-intermediate for 1200 s, and Mn-poor for 920 s). In the case of the Sn-rich TF, the deposition time was 2100 s for Sn, 710 s for Cu, and 1200 s for Mn. The second series of samples was produced using as reference the Mn-poor regime (1450 s for Sn, 510 s for Cu, and Mn for 920 s), and the deposition times were increased of 15%, 30% and 50%.

Then, the metallic stacks have been sulphurised in a graphite box containing 0.06 g of sulphur. The box was moved in a quartz tube, which was placed in a tubular oven heated in argon flow with a two-step temperature program: the first step at 550 °C for 3 min to avoid furnace overshoot (ramp 15 °C/min), and a second step at 570 °C for 40 min (ramp 6 °C/min), followed by natural oven cooling down to room temperature (down to RT with an average cooling rate of about 1.5 °C/min). In selected samples, a chemical etching in an aqueous solution (3% v/v) of hydrochloric acid (HCl) at 75 °C for 10 min was performed to clean the CMTS TF surface from the soluble secondary phases. Four other layers have been deposited on top of Mn-based chalcogenide TFs to produce the CMTS solar cells. First, an 80 nm buffer layer of cadmium sulphide (CdS) has been deposited on the etched CMTS films by chemical bath deposition (CBD), following the procedure published by some of the authors elsewhere [43]. Then, a 50 nm layer of intrinsic zinc oxide (i-ZnO) and a 300 nm thick layer of aluminium-doped zinc oxide (AZO), used as front contact of the CMTS PV device, have been sputtered on CdS. Finally, an aluminium grid was thermally evaporated on top of the full stack of the layer as a charge collector [44,45]. Each single PV device was insulated on the Mo-back contact by mechanical scratch following the pattern shown in Fig. S1, obtaining a final device with an active area of 0.3 cm^2, doubling the previous record device area [40]. JV measurements with and without a black mask (Fig. S2) confirm that the individual solar cells are electrically isolated. A post-finalization process based on thermal treatment of the full device in air, performed on a thermostatic plate at 260 °C for 10 min (ramp 9 °C/min), has been introduced to improve the final PV performance of the CMTS solar cell. The devices were stored in the dark, kept at RT, and with a relative humidity between 25% and 55% over the seasons.

To investigate the CMTS properties, several samples have been produced as a function of final composition and thickness. Except for the UV–Vis spectroscopic measurements carried out on CMTS TF grown on SLG, all the other characterizations have been performed on Mo-coated SLG substrates. Before the CdS buffer layer deposition, small portions of CMTS TFs have been analysed via Scanning Electronic Microscopy (SEM: Tescan Mira3 FEG) both morphologically and compositionally, exploiting the energy dispersive x-ray spectroscopy (EDX, EDX: Bruker Quantax Compact – electron acceleration = 20 keV). Being the S and Mo main picks overlapped in EDX spectra, the chalcogenide layers have been partially scratched to remove small flakes from the Mo-back contact to be analysed by SEM/EDX, giving a reliable EDX evaluation of the sulphur amount in CMTS TFs. Exploiting the random distribution of these free-standing flakes dispersed on the rest of the CMTS TF surface, at the same time it is possible to i) study the morphology of the interface between chalcogenide and Mo-back contact (face-down flakes); ii) check the grain structure along the section of the CMTS layer (orthogonally oriented flakes); iii) measure the EDX composition on flakes bundles, so increasing the total thickness of the chalcogenide thin film to minimize the Mo signal and have a reliable evaluation of the sulphur percentage. Quantitative evaluation of the secondary phases has been used for relative comparison between samples. Then, CMTS TFs have been grinded, and the powder has been put on a misoriented Si holder to eliminate the Mo signal from the XRD patterns, obtained by using a Bruker D2 PHASER with a linear detector. XRD picks analysis and the identification of the crystalline phases have been carried out by the PDF4+ database (ICDD). CMTS samples have been furthermore characterized by Raman spectroscopy (Jasco Ventuno μ-Raman), equipped with a Peltier-cooled charge-coupled device camera (operating temperature: −50 °C) and a He–Ne laser (wavelength 632.8 nm), and UV–Vis transmittance measures (Jasco V-570, range 250–2500 nm). PV devices have been characterized with Solar Simulator I–V measures, by a 500 W Xe light source (ABET Technologies Sun 2000 class ABA Solar Simulator), that was calibrated to 1.5AM at 1000 W/m^2 by a reference Si cell photodiode (RR-103-O RERA SYSTEMS) provided with an IR cut-off filter (KG-5, Schott). External Quantum Efficiency measurements (SpeQuest quantum efficiency system equipped with an Omni 300 LOT ORIEL monochromator, single grating in Czerny–Turner optical design, AC mode with a chopping frequency of 88 Hz) were also performed. Photoluminescence, PL, data were collected using a single grating monochromator (Jarrell-Ash) in the 700–1700 nm spectral range and a

spectral resolution of 6.6 nm, using a standard lock-in technique with a short wavelength enhanced InGaAs detector (maximum responsivity at 1540 nm). A laser with excitation wavelength $\lambda_{xc} = 405$ nm (Crystalaser) and a pump power of 90 mW was used. A cooling system consisting of a rotary pump, a turbomolecular pump and a He closed-circuit cryostat was used to perform PL measurements from 15 K to RT. X-ray photoelectron spectroscopy (XPS) measurements have been performed by mean of a Kratos Analytical AXIS Ultra DLD spectrometer, equipped with an achromatic Mg Kα/Al Kα dual anode X-ray source and a monochromatic Al Kα one. The monochromatic Al Kα anode (1486.6 eV) was operated at 150 W and 15 kV. The 180° hemispherical energy analyzer with an average radius of 165 mm was operated using a hybrid lens mode at pass energy of 160 eV for survey spectra and 20 eV for region spectra. XPS spectra were recorded at a take-off angle of 90° from the surface of the sample holder using an aperture slot of 300 × 700 μm^2. Samples were mounted on a stainless-steel sample bar (130 × 15 mm^2). The relative atomic concentrations of the elements were determined from the appropriate integrated peak areas at the core level and the sensitivity factors provided by the original analysis Kratos Vision 2.2.10 software. The Shirley background subtraction was used to calculate relative atomic concentrations. No charge correction was applied to any energy scale as the samples were conductive enough. Admittance spectroscopy (AS) data have been collected by using Biologic SP-240 potentiostat in 2-probe configuration (amplitude of the superimposed AC potential 50 mV, V_{bias} ranging from −1.5 to 2.0 V with a step of 50 mV, frequency ranging from 1 MHz to 100 Hz with 6 points per decade). Data analysis has been made utilizing OriginPro 2021. Vesta software has been used to draw the 3D crystal structure of some secondary phases identified in CMTS TFs.

3. Results and discussion

In CZTS TFs a Cu-poor, Zn-rich condition ([Cu]/[Zn]+[Sn]≈0.8, [Zn]/[Sn]≈1.2, [Cu]/[Sn]≈1.8 [46]) is usually employed to obtain high-efficiency solar cells. This condition impacts the PV performances enhancing the charge conductivity and avoiding the formation of deep trap levels [47]. However, these compositional constraints could be not valid for CMTS, due to the atomic arrangement being different from those adopted by CZTS [34,40]. Rudisch, indeed, demonstrated that the most stable crystal structure for CMTS is stannite [35], meanwhile, CZTS is settled in the kesterite phase. Stannite and kesterite are two polymorphs with small energy differences [48]. The discrepancy between CMTS and CZTS is also highlighted by the different kinetics of the secondary phase formation: CZTS TFs usually have as by-products binary and ternary sulphides (e.g. Cu_{1-x}, ZnS), meanwhile, in CMTS TFs the formation of quaternary sulphides, such as $Cu_2MnSn_3S_8$, is also detected [34,35,40]. Therefore, the compositional range is tuned, varying the Mn and Sn content of the first series of CMTS TFs in a Cu-poor regime ([Cu]/[Mn]+[Sn] < 1). Table 1 summarizes the atomic concentrations (% at.) of metallic elements (identified via EDX measurements) and the related compositional ratio for all the synthesised samples. A strong adhesion at the substrate (with and without Mo layer) and a S content higher than 50 %at. have been observed, indicating a successful sulfurization process. Composition measurements have been carried out both on the CMTS TF surface (front) and at the back interface with Mo (EDX measure on flakes): the recorded variations are negligible, and they can be ascribed to the variability in the experimental data and the intrinsic limits/resolution of the EDX technique (data variation evaluated of ±0.5%). The SEM images are presented in Fig. 1. The top view is quite alike for all the samples: a highly homogeneous multi-crystalline surface has been observed without evidence of secondary phase segregation. Cross-section images show that the TFs (thickness ranging from 650 nm to 700 nm) are compact and composed of large grains on the top and smaller ones at the bottom. The SEM analysis of the CMTS/Mo interface (rear) confirms the presence of voids: these are extended defects well known in CZTS TFs grown with a two-step approach similar to that exploited in this work [49]. This phenomenon has been observed many years ago by Smigelskas [50] during copper sulfurization. The void formation has been associated with the different diffusion rates of the metallic atoms towards the surface. The voids shape, dimension and density distribution at the rear surface of CMTS samples studied in this work are similar to those detected in CZTS TFs grown by the same process [49].

The crystalline phases identified in CMTS TFs have been quantified by exploiting the Rietveld refinement of the XRD pattern via TOPAS software, and the values of their weight concentrations (wt.%) are compared in Table 1. Sn-rich sample (**CMTS.04**), is compositionally similar to the Mn-poor compound and shows the same secondary phases present in **CMTS.02** with just an increase of the Sn-rich thio-spinel phase $Cu_2MnSn_3S_8$. Therefore, the last has been identified as the secondary phase presents also in the **CMTS.03** sample, where the Mn excess is compensated with the increase of MnS percentage, as estimated by the Rietveld refinement. Fig. 2 shows the XRD patterns of the first series of CMTS TFs: **CMTS.01**, **CMTS.02, CMTS.03**, and **CMTS.04** samples. The peaks analysis reveals the formation of CMTS with stannite structure (spatial group Pmn21, PDF4+ card 00-051-0757) in **CMTS.02** (Cu and Mn-poor), where the main peak is the (1 1 2) direction at 28.21°. The presence of reflections additional to those typical of CMTS in the TFs grown in Mn-rich and Mn-intermediate regimes, respectively **CMTS.01** and **CMTS.03**, has been revealed. **CMTS.04** shows a pattern very similar to **CMTS.02**, except for the signal at 49.5 °C related to both main secondary phases identified exploiting the PDF4+ (ICDD) database. Those additional reflections have been linked to manganese sulphide (MnS) with alabandite structure (card 00-006-0518) in the case of Mn-rich regime (**CMTS.01**), and to a quaternary sulphide with thio-spinel structure in the case of Mn-intermediate sample (**CMTS.03**). Both these secondary phases are known to be typical CMTS by-products [22,24,35], and they have peculiar XRD picks, 29.2° (MnS) and 45.2° ($Cu_2MnSn_3S_8$), which aids in the phase identification.

In literature, $Cu_{0.92}Mn_{0.5}Sn_{1.5}S_4$ (card 00-051-0664) formulation is attributed to the thio-spinel $Cu_2MnSn_3S_8$, and it is identified as a by-product in CMTS TFs [34,35]. A deeper analysis of XRD data has shown that the same diffraction pattern is common for other Cu–Mn–Sn–S thio-spinels formulations [51]. In particular, $Cu_2MnSn_3S_8$ shares the same lattice parameters and structures with $Cu_{0.5}Mn_{1.5}SnS_4$ (card 04-003-8291) and $Cu_{0.5}Mn_{1.25}Sn_{1.25}S_4$ (card 04-003-8287). In Fig. S3, the 3D structures of the three thio-spinels have been compared to appreciate how the same crystalline structure can manage to arrange

Table 1
CMTS samples of the first series and their compositional ratios (metallic element, %at., with data variation = ± 0.5%; and relative metal ratios with data standard deviation = 0.03%). Sulphur is higher than 50 %at. in all the samples, so it has not been included in the table. For each sample the weight percent (wt%) for each crystalline phase is reported (quantified by Rietveld analysis).

Cu-poor sample		% at. Via EDX			Compositional ratio			wt% via Rietveld on XRD data [PDF4+ database code]		
		Cu	Mn	Sn	Cu/Mn + Sn	Mn/Sn	Cu/Sn	CMTS [04-012-0329]	Thio-spinel [04-003-8287]	MnS [00-006-0518]
CMTS.01	Mn-rich	44.4	32.9	22.7	0.80	1.47	1.98	90	/	10
CMTS.02	Mn-poor	47.2	27.0	25.8	0.89	1.05	1.83	95	4	1
CMTS.03	Mn-intermediate	44.6	29.5	25.9	0.81	1.14	1.72	85	9	6
CMTS.04	Sn-rich	47.6	25.1	27.3	0.91	0.92	1.75	93	6	1

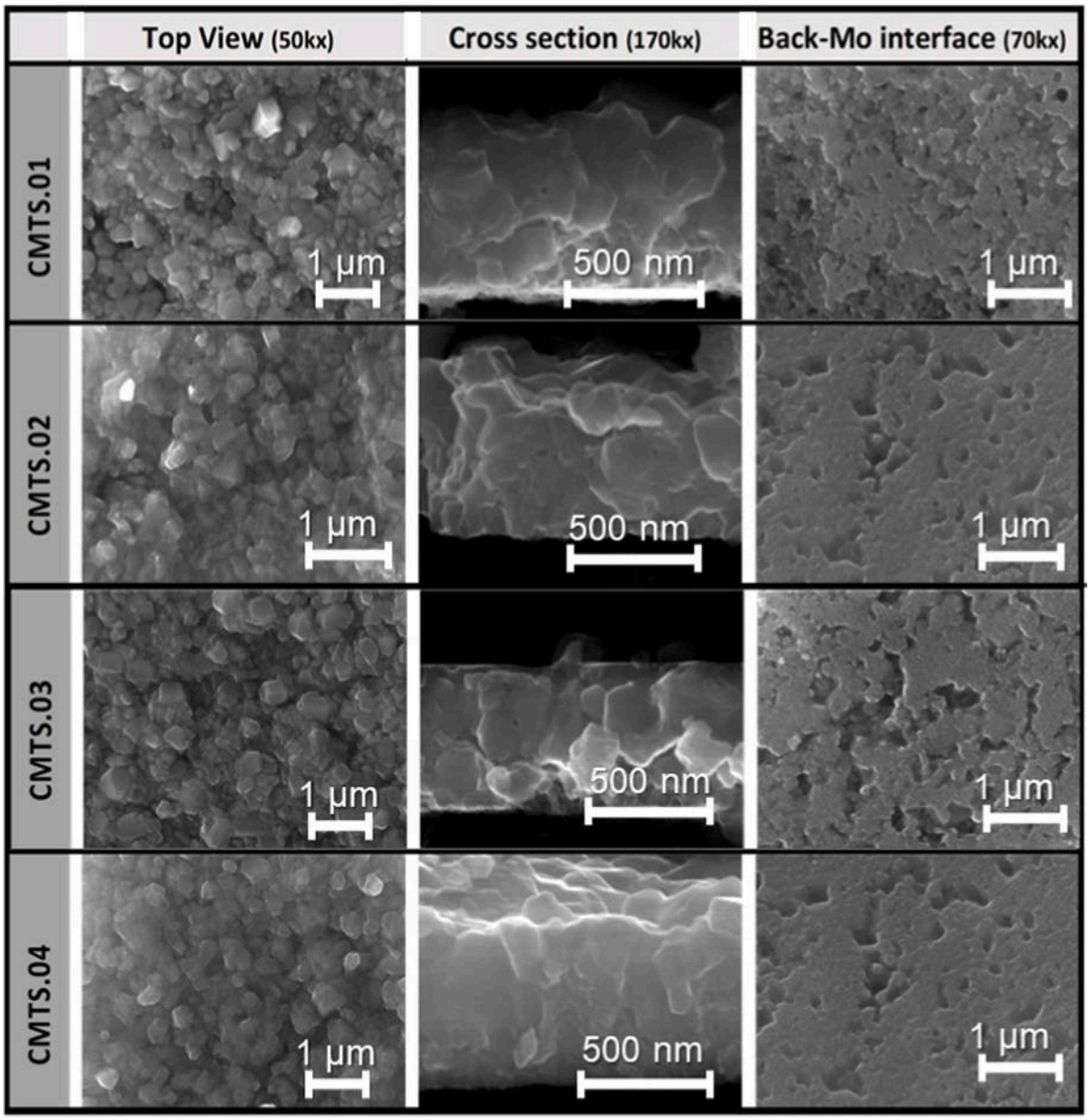

Fig. 1. SEM images of the first series of CMTS TFs: the TF morphology (top view images), the cross-section, and the interface with Mo-back contact have been checked.

in different formulations, ranging from Mn-rich to Cu-rich regimes, just adapting the occupancy values and the elements in the cationic lattice sites. To further investigate the recorded secondary phases, Raman spectra with a 633 nm laser have been collected for the three samples grown in different Mn-regimes. Fig. 3 displays the detailed analysis of the experimental Raman spectra for three representative samples. The TF in the stannite structure showed the CMTS distinctive peaks positioned at 252 cm^{-1}, 282 cm^{-1}, 303 cm^{-1}, 331 cm^{-1}, 349 cm^{-1} and 365 cm^{-1} [27], nicely in accordance with the published literature [34,40]. Fig. 3a shows the first and the second-order Raman emissions [34], and Fig. 3b is an enlargement of the first-order raw data, compared with the deconvoluted peaks and the cumulative fit peak. In both **CMTS.01** and **CMTS.03** (Fig. 3b), a peak around 260 cm^{-1} arises. The MnS presence is reported to be revealed by peaks at 260 cm^{-1}, 300 cm^{-1} and 655 cm^{-1} [34]; unfortunately, the last peaks overlap with peaks of the main phase. Therefore, only the shoulder at about 260 cm^{-1} could be considered to reveal the alabandite presence. The peak at 295 cm^{-1} appears only in the Mn-rich sample (**CMTS.01**), and it could be related to tetragonal-Cu_2SnS_3 [52], induced by the high concentration of the MnS secondary phase detected in the sample.

The peak located at 350 cm^{-1} in **CMTS.01** and **CMTS.02** seems to split into two in the samples where the highest thio-spinel quantity has been estimated via Rietveld refinement (**CMTS.03**): one small contribution at 348 cm^{-1} and a large one at 353 cm^{-1}. The two peaks have been reported by Rudisch for samples containing both Cu_2MnSnS_4 and $Cu_2MnSn_3S_8$ phases [35]. Therefore, Raman analysis identifies stannite as the main phase in Cu- and Mn-poor samples (**CMTS.02**) and finds that it is combined with alabandite in samples grown in the Mn-rich regime (**CMTS.01**). On the purest CMTS sample (**CMTS.02),** Raman emission measurements have been carried out both with 532 nm and 633 nm laser (Fig. S4): the spectra are in agreement with the published literature [35]. UV/Vis measurements have been carried out on TFs grown on SLG to estimate the optical band gap. Chen Leilei et al. [22] reported E_g values that vary from 1.2 to 1.6 eV by changing the annealing time at high temperatures; Cui reported 1.3 eV using wet chemistry preparation from nano-powders [17]; Rudisch reported E_g values in the range

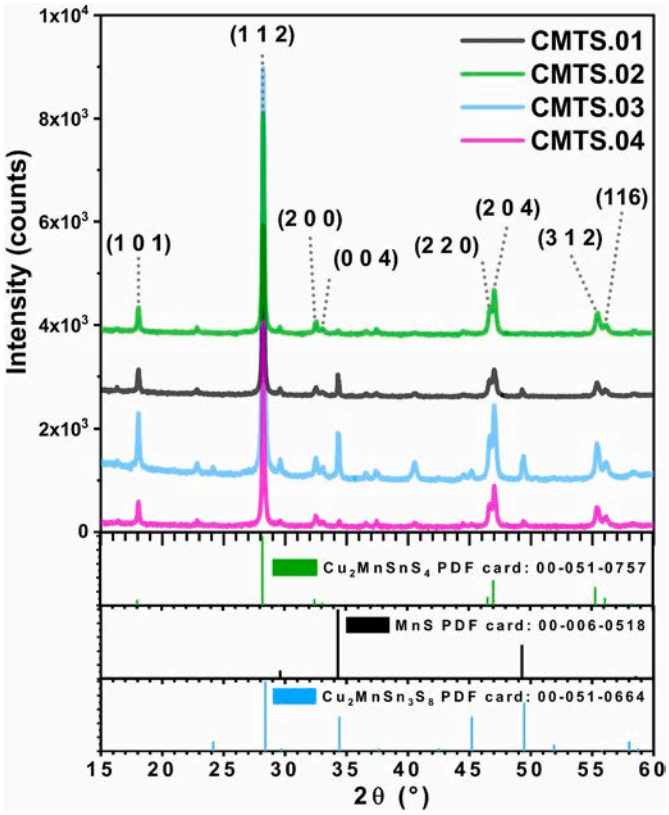

Fig. 2. XRD patterns of CMTS.01, CMTS.02, CMTS.03, CMTS.04 together with the peaks' attribution, compared with the PDF cards of stannite-Cu_2MnSnS_4, alabandite-MnS, and thiospinel $Cu_2MnSn_3S_8$.

1.4–1.6 eV for reactive sputtering samples [35]. As shown in Fig. 4a, **CMTS.01** (Mn-rich sample) has an optical E_g of 1.6 eV, **CMTS.02** and **CMTS.03** about 1.55 eV, in line with the literature for the sputtering method [22]. The absorption linear region to be considered for the E_g calculation was evaluated considering the absorption coefficient α in Fig. 4b.

Identified the Cu- and Mn-poor regime as optimal to minimize the presence of secondary phases, we deposited the second series of CMTS TFs gradually increasing the final thickness. Indeed, **CMTS.02** was just about 650 nm thick (Fig. S2): this is still too far from the optimum value for PV application, which, taking into account the CMTS absorption coefficient exceeding 10^5 cm^{-1} (Fig. 4b), should range from 1.2 μm to 1.5 μm [53]. The thickness has been increased extending the deposition time of Sn, Cu and Mn (Sn: 1450 s; Cu: 510 s; Mn-poor: 920 s) respectively by +15% (**CMTS.02 + 15%**, ≈740 nm thick, Fig. 5a), +30% (**CMTS.02 + 30** series, ≈825 nm thick, Fig. 5b) and +50% (**CMTS.02 + 50** series, ≈945 nm thick, Fig. 5c). A further increase in deposition time has not been performed to avoid the Sn target overheating.

CMTS TFs morphology do not seem to be affected by the final thickness increase (Fig. S5), and no segregation of secondary phases on top has been observed. At the Mo-interface, a small reduction of the dimension of the void, a shift of their aspect ratio toward 1 and a more homogenous spatial distribution have been observed as the film thickness increases. Also, the Raman spectra confirm that the main phase present in the compounds is stannite (Fig. S6). Metals' ratio fluctuations of about ±0.05 have been measured, but this range has been considered compatible with the EDX measurements and the intrinsic limit of the deposition method. A variability of ±0.5% of the atomic concentration has been estimated for EDX measurements. The sputtering main limit is the deposition time when metals with a low melting point are involved. In CMTS, the Sn source can be affected by fluctuations in the deposition flux, which can be more evident the longer the deposition lasts. A gradual overheating can alter the Sn flux, with a higher impact on a small target as the one employed in this work. Rietveld refinement (Table 2) highlights slight variation in the percentage of secondary phases as a function of the metals' ratio fluctuation discussed before. For all the samples of the second series a CMTS wt% higher than 92 has been estimated.

Prototypal solar devices based on the second series samples have been produced, exploiting the standard CZTS-like architecture [41,45]. In this work, the effects of post-deposition treatments (PDTs), already successfully employed in CZTS [54–56], have been tested to enhance the CMTS PV performances. Two different PDT processes have been compared: a thermal process and a chemical one. During the thermal treatment (TT) the CMTS devices are heated on a hotplate at 260 °C for 10 min in air. In Fig. 6, the PV parameters before and after TT are compared: without TT, PV efficiencies barely exceeded 0.1%. In general, the increase in CMTS thickness appears to induce a modest improvement in the overall performance of the solar cells, even if the values without TT are too low to support a reliable analysis. When the TT is applied, a remarkable improvement of PV efficiencies for the thicker samples (**CMTS.02 + 30%** and **CMTS.02 + 50%**) has been measured, mostly thanks to the V_{oc} significative increase (up to +400%) in both cases. TT had a more severe impact on **CMTS.02 + 50%** Jsc and FF than on those of **CMTS.02 + 30%**. Raman measurements carried out directly on the CMTS champion device before and after TT are quite alike, as highlighted by the peaks deconvolution reported in the supporting information (Fig. S7). In CZTS and CZTSe, the PV performance increase after the TT is combined to a red-shift of the main A-mode (338 cm^{-1} and 197 cm^{-1}, respectively) [55,57], due to the rearrangement of Cu/Zn-order [55], and to the interdiffusion of Cd in the absorber layer (appearance of the Raman peak of $Cu_2Zn_{x-1}Cd_xSnS_4$ structure at 332 cm^{-1}) [57]. But, neither the A-mode red-shift nor the appearance of a peak close to the CMTS A-mode (331 cm^{-1}) has been registered in the Raman spectra (Fig. S7). But Neuschitzer and coworkers also find out (through a detailed analysis of transmission electron microscopy images and electron energy-loss spectrometry measurements) that, after the TT of the CTZSe solar cells, the grain boundaries' composition moves to a Cu-poor and Zn-rich configuration, and a large amount of Cu droves inside the CdS layer [57]. Therefore, it is reasonable to conclude that during the TT the Cu diffusion happens at the CMTS/CdS interface, where the Cu leaves the this interface in a Cu-poor and Mn-rich configuration and simultaneously acts as a dopant in the CdS buffer layer.

For the **CMTS.02 + 50%,** the TT has been combined with an HCl chemical etching of the CMTS surface before the CdS deposition. The HCl etching without TT does not significantly improve the PV efficiency, even if an improvement of CMTS TFs quality has been observed by the XRD analysis (Fig. S8). In the XRD patterns collected for **CMTS.02 + 50%** samples, most of the peaks attributed to the thio-spinel and MnS secondary phases disappear after the acid treatment (Fig. S8). The implementation of both treatments (HCl + TT) improves the PV performance: the maximum efficiency delivered by the freshly produced CMTS devices was 0.65%. Fig. 7a shows the JV characteristic curves before and after TT: the V_{oc} jumps from 119 mV to 420 mV, the J_{sc} increases from 3.77 mA/cm^2 to 4.56 mA/cm^2, and the FF shifted from 29.72% to 33.94%, increasing of five times the final efficiency (from 0.13% to 0.65%).

The external quantum efficiency (EQE) curves before and after TT are presented in Fig. 7b: TT increased the EQE in the range of 550–800 compared to the EQE before TT. Already observed for CZTS solar cells after TT, this enhancement in CZTS solar cells has been attributed to a decrease in charge recombination within the depletion zone, and an increase in charge carrier lifetime [55]. A slight downhill before TT is visible in the range of 600–800 nm, partially restored by the TT: this effect is reported in a previous work of the group [40], and it could be correlated to the presence of bulk defect bleached by the TT. Furthermore, the absorption edge is sharper after the TT, indicating an enhanced charge extraction [57]. The EQE loss after TT for wavelengths

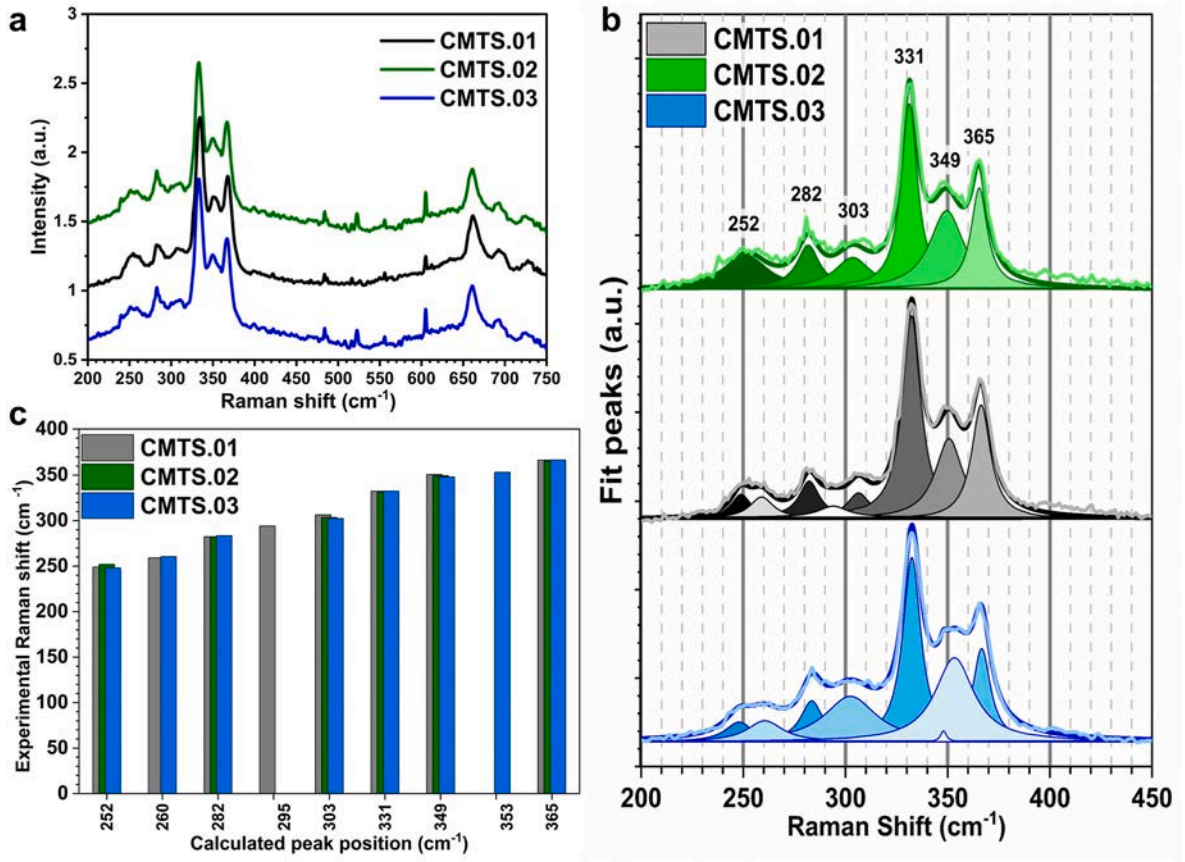

Fig. 3. **(a)** Raman raw data of **CMTS.01**, **CMTS.02**, **CMTS.03** reporting the first and second scattering order; **(b)** first order peaks deconvoluted from Raman spectra and cumulative fits peak (**CMTS.01**: R-Square = 9.91E-01; **CMTS.02**: R-Square = 9.94E-01; **CMTS.03**: R-Square = 9.96E-01) overlapped to the raw data; **(c)** Experimental Raman shifts versus calculated peak position in **CMTS.01**, **CMTS.02**, **CMTS.03**.

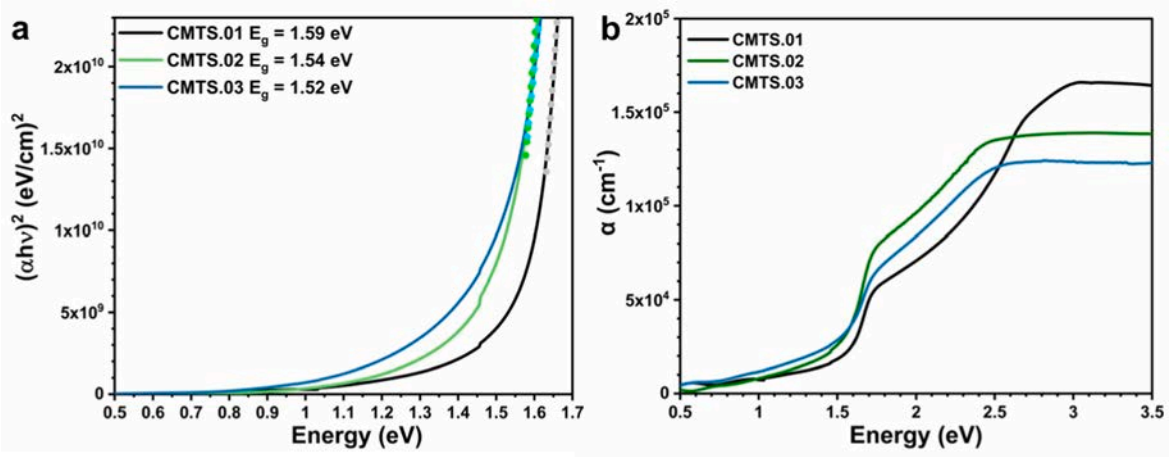

Fig. 4. (**a**) Tauc plots of **CMTS.01**, **CMTS.02** and **CMTS.03** series (calculated E_g is reported in the legend); (**b**) **CMTS.01**, **CMTS.02** and **CMTS.03** absorption coefficient (α).

less than 530 nm has already been reported for CMTS, and it has been attributed to an increase in the CdS parasitic absorption [40]. The red shift, visible at the maximum around 550 nm, and the reduction of the CdS-related plateau could be explained by the diffusion between the buffer layer and the layers sandwiching it [57–59]. The band gap shrinking after TT, reported for CZTS (130 meV) and attributed to the partial replacement of Zn by Cd [55], is not registered in the CMTS/CdS device (Fig. 7c). Therefore, Mn partially replaced by Cd seems to be negligible, and the sharper EQE edge of **CMTS.02 + 50%+HCl + TT** compared to **CMTS.02 + 50%+HCl** could be attributed to a defect concentration reduction at the CMTS/CdS interface [60]. The PV performance of the double-treated (HCl + TT) champion solar cell has been periodically measured to check its stability over time. The device was stored in the dark, at RT, and with humidity ranging from 25 RH% to 55 RH% over the seasons. Surprisingly, the device is still improving its PV performances almost doubling the efficiency in just over a year from the first measurement: the JV characteristic curves and EQE recorded over the time are summarised in Fig. 8 and Table 3.

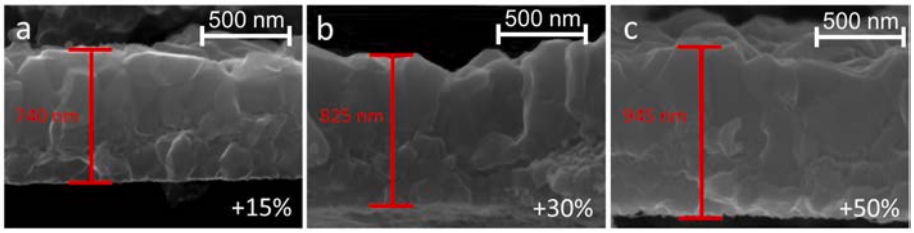

Fig. 5. Cross-section SEM images of CMTS TFs deposited with an increase of +15% (a), +30% (b), and +50% (c) of the metals' deposition time, taken CMTS.02 as reference. Respectively, the measured thickness is 740 nm, 825 nm and 945 nm.

Table 2
CMTS samples of the second series and their compositional ratios (metallic element, %at., with data variation = ± 0.5%; and relative metal ratios with data standard deviation = 0.03%). Sulphur is higher than 50 %at. in all the samples, so it has not been included in the table. For each sample the weight percent (wt %) for each crystalline phase is reported (quantified by Rietveld analysis).

	Compositional ratio			wt% via Rietveld on XRD data [PDF4+ database code]		
	Cu/Mn + Sn	Mn/Sn	Cu/Sn	CMTS [04-012-0329]	Thio-spinel [04-003-8287]	MnS [00-006-0518]
CMTS02 + 15%	0.90	1.06	1.89	93	5	2
CMTS02 + 30%	0.90	1.02	1.84	92	7	1
CMTS02 + 50%	0.91	1.07	1.87	95	4	1

EQE recorded in over a year is enhanced overall in the spectral range, suggesting further spontaneous curing. Few reports discuss this phenomenon in chalcogenide-based solar cells: the efficiency improvement with ageing in CIGS/CdS solar cells has been associated with the increased doping density in the space charge region, due to Cu migration [61], or an increase of the barrier at the Mo-back contact [62]; meanwhile in CZTS/CdS solar cells this behaviour, observed in highly ordered structures, has been correlated to a spontaneous increase of the cations disorder followed by an E_g lowering [65,66]. No significant difference has been detected in the band gap of the CMTS-aged device over time (Fig. 8c). Such an increase all over the working spectral range seems to be related to a charge recombination decrease, a charge carrier lifetime increase, and a more effective charge separation [55,60]. The analysis of the shunt resistance (R_{SH}) and series resistance (R_S) evolution (Fig. 9) can provide additional information: these two parameters can be extrapolated from the slopes of the characteristic curves (Fig. 8a), where the voltage and current are null, respectively [63,64]. The R_{SH} plotted values show no variation in the first semester and only a slight decrease in the last semester. This is consistent with the almost constant FF values

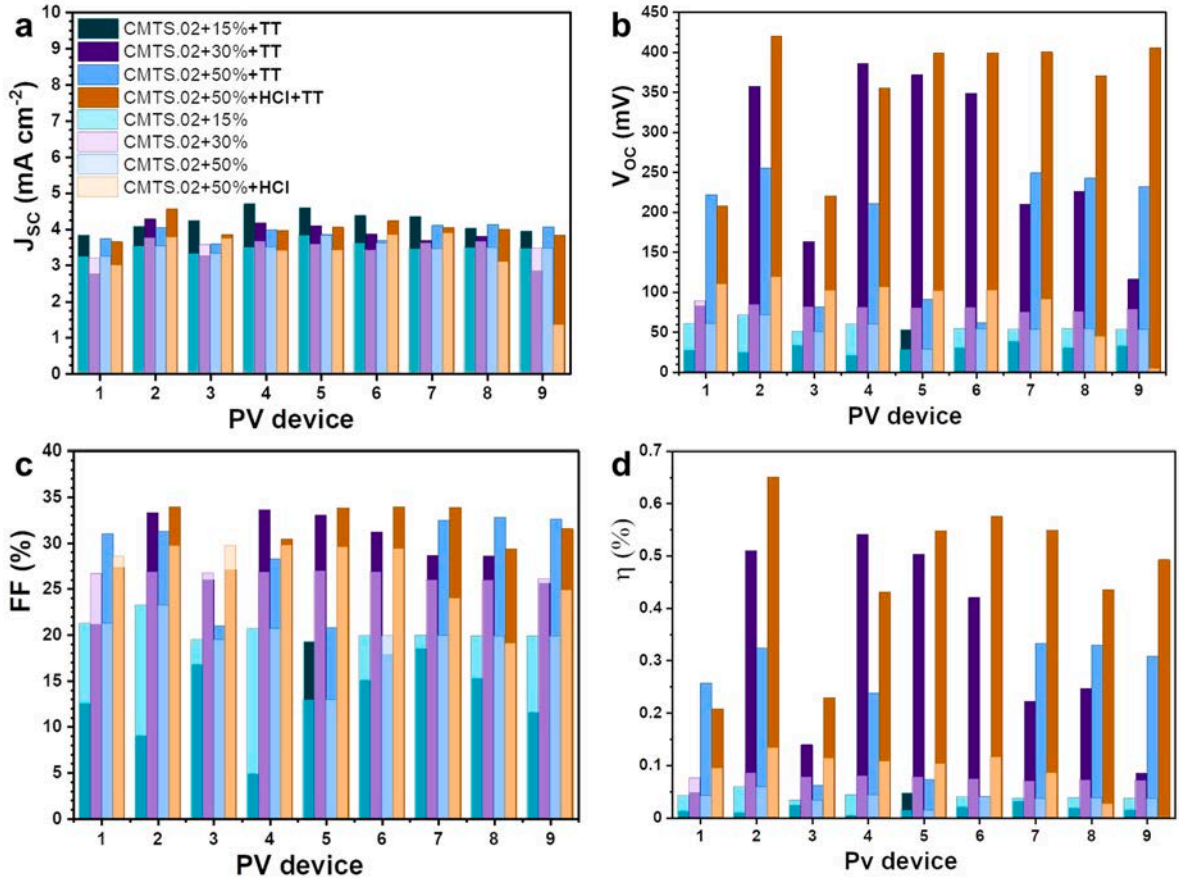

Fig. 6. Column chart of device performance parameters based on the nine samples of the second CMTS series.

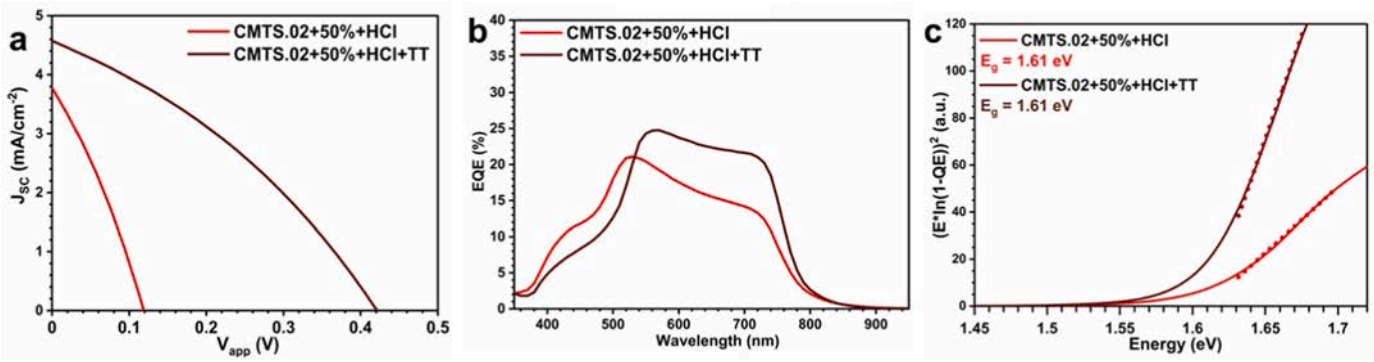

Fig. 7. (**a**) J-V curves of the champion device, before and after the thermal treatment (TT); (**b**) EQE measures made on the champion device, before and after TT; (**c**) E_g calculated from EQE measurements before and after TT.

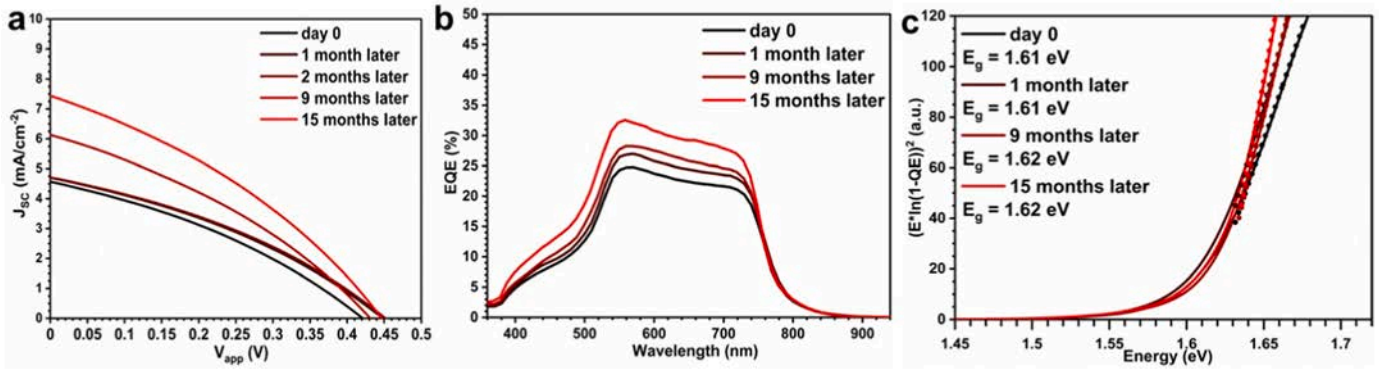

Fig. 8. (**a**) J-V curves of the champion device, obtained with **CMTS.02 + 50%+HCl + TT** and recorded in 15 months; (**b**) EQE measures made on the champion device recorded in 15 months; (**c**) E_g calculated from EQE measurements recorded in 15 months.

Table 3
CMTS.02 + 50%+HCl + TT champion device PV parameters recorded in 15 months.

	J_{sc} (mA/cm^2)	V_{oc} (mV)	FF	η (%)
day 0	4.56	420.41	0.34	0.65
1 month later	4.70	447.83	0.34	0.72
2 months later	4.71	451.14	0.35	0.74
9 months later	6.14	430.89	0.34	0.89
15 months later	7.45	444.80	0.34	1.13

in Table 3, indicating no variation in leakage current over time [64]. R_S seems to have two trends: an initial faster improvement and a second one that occurs over a longer time scale. Therefore, we can suggest that ageing improvement mainly concerns R_S. The rapid initial reduction may be due to the Cu drift, and the slower one could be due to a spontaneous defect passivation reducing the charge recombination at the various device's interfaces. A more systematic study should be conducted, above all by verifying whether the phenomenon is also common to devices with performances higher than 10% PV efficiency.

To better understand which could be the defects at stake, PL measurements have been carried out on **CMTS.02 + 50%+HCl** and **CMTS.02 + 50%+HCl + TT** after 5 and 9 months, varying excitation power and temperature [65–67]. The PL emission of **CMTS.02 + 50%+HCl** after 9 months was in the order of the background noise; therefore, it was not possible to make a reliable assessment. On the other hand, The PL spectra of **CMTS.02 + 50%+HCl + TT** after 9 months are reported as a function of the temperature and the excitation power in Fig. 10a. The bands have the typical asymmetrical shape and show the evolution of two bands: D1 at 1.30 eV and D2 at 1.10 eV. Increasing the temperature, the PL peak D1 slightly moves to lower energies but, above all, is

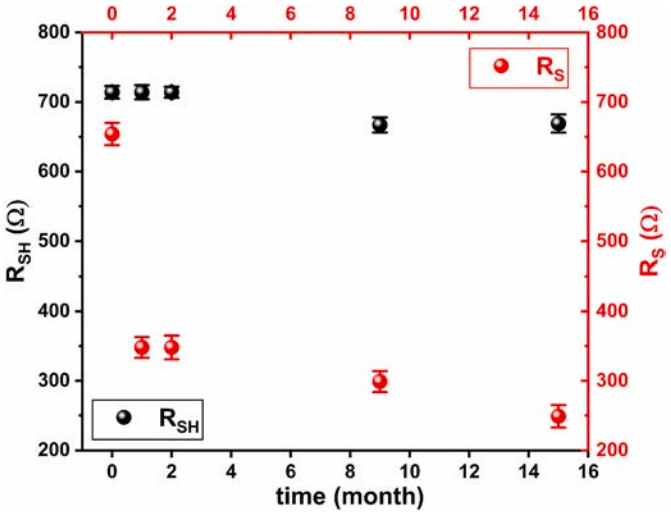

Fig. 9. Shunt resistance (R_{SH}) and series resistance (R_S) of CMTS.02 + 50% + HCl + TT were evaluated as a function of the PV device ageing by assuming the single diode model.

almost quenched for temperature above 200 K, where the main contribution comes from peak D2. The band D1 could be ascribed to the deep recombination centres identified in CZTS: ($2Cu_{Zn}^{-} + Sn_{Zn}^{2+}$) clusters acting as deep wells, and giving a discrepancy between the energy gap and the PL peak position [68]. The hypothesis is also confirmed by the D1 quenching at high temperatures, as it has been reported for CZTS [68]. Therefore, we can suggest that the D1 band could be linked to ($2Cu_{Mn}^{-}$ +

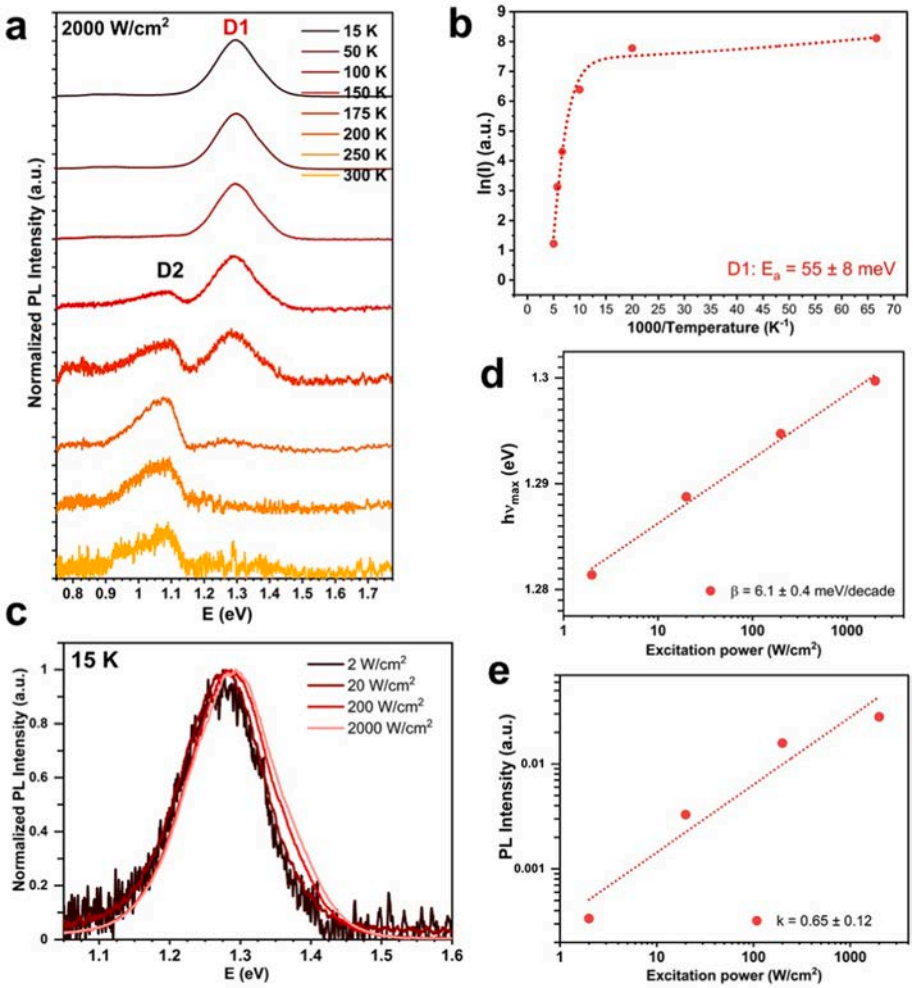

Fig. 10. PL analysis of the champion device after an ageing of 9 months: (a) spectra at full power varying the temperature; (b) temperature dependence of the integrated intensity; (c) spectra at T = 15 K varying the excitation power; (d) peak position dependency on the excitation power at T = 15 K; (e) intensity dependency on the excitation power at T = 15 K.

Sn_{Mn}^{2+}) clusters inducing potential wells for holes and electrons, so increasing the recombination between holes in the valence band maximum and electrons in the conduction band minimum. D2 band has already been observed in CMTS TFs, and it has been attributed to deep defects [34], in which the emission is activated by the rising temperature. The fitted temperature dependency of the integrated PL intensity, Fig. 10b, reveals that the D1 thermal activation energy is 55 ± 8 meV [65,66,69], suggesting that the defect can act as an efficient recombination centre. PL measurements, performed at 15 K varying the excitation power (Fig. 10c), show a blue shift increasing the laser power with a rate of 6.1 meV/decade (Fig. 10d). The registered peaks are presented in Fig. S9. This suggests a moderate disorder, comparable with the zinc-substituted compounds [66,70]. The power coefficient *k* in Fig. 10d, calculated by the linear fit of the PL intensity dependence by the excitation power, is a value related to the power conversion efficiency and it is lowered by the defects present in the bandgap. A *k* lower than one, such as 0.65 in CMTS, confirms that detrimental energy levels are localised within the bandgap, giving rise to radiative recombination [65,66,69,70]. The cation disorder occurrence, caused by the formation of antisite defects, leads to fluctuations in the optoelectronic properties, especially in the energy gap (E_g), limiting the final efficiency of the related devices [71,72]. It is commonly accepted that cation substitution with metals with higher ionic radius, like for Mn, in this case, limits the formation of these antisite defects due to higher formation energy, even if the observed effects are minimal. Yuan et al. [73] studied theoretically the substitution of Cu with Ag and Zn with Cd to suppress the formation of antisite pairs, and Timmo et al. [74] studied this double substitution in the sulphur-selenide material; however, Chen et al. [75] simulated the substitution of Zn with a lot of metals (Be, Mg, Ca, Mn, Fe and Ni), concluding that the formation energy of antisite pairs in this materials are very similar. The results reported here could confirm Chen's calculation [75], suggesting that also CMTS must deal with these recombination states. On the other hand, the D2 band's low intensity for temperatures below 200 K impacts the fitting reliability, and no speculations can be done.

X-ray photoelectron spectroscopy, XPS, has been used to identify the oxidation state of all the compound's elements. The measurements have been performed on a **CMTS.02 + 50%+HCl** twin sample grown on an Mo-coated SLG to avoid any contaminations coming from the top layers constituting the solar cells and applying a plasma etching for 120 s, 480 s, and 1200 s. The high-resolution XPS Cu 2p spectrum (Fig. S10a) shows two peaks at about 952 eV (Cu $2p_{1/2}$) and 932 eV (Cu $2p_{3/2}$): the peak splitting of 20 eV confirms the Cu^{+1} state as reported for CMTS [76,77]. The manganese survey is more complex to be analysed: Mn can assume many oxidation states (ranging from +2 to +7, where the most common ones are +2, +4, and +7) [78]. Fig. 11b can be deconvoluted to eight peaks [76,77]: Mn $2p_{1/2}$ (653.0 eV) and Mn $2p_{3/2}$ (641.0 eV), with peak splitting of 12 eV confirming Mn^{+2} state as reported for CMTS [76,77]; Mn^{+3} as reported for Mn_3O_4 (651.0 eV and 640.0 eV) [79,80]; Mn^{+4} with the main photoemission lines at 654.0 eV and 642.0 eV, and with

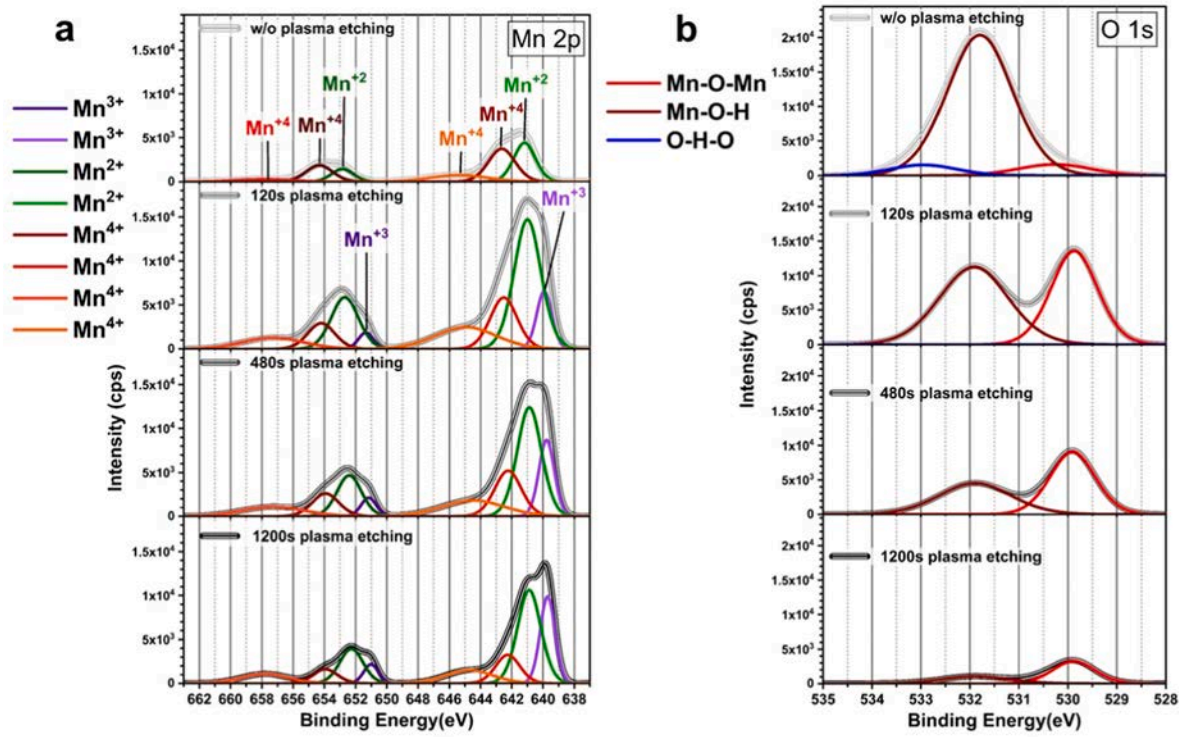

Fig. 11. High-resolution XPS spectra of (**a**) Mn 2p and (**b**) O 1s.

the two spin–orbit split peaks at 658.0 eV and 645.0 eV as reported for MnO_2 [81,82]. The two peaks in the Sn 3d core level spectrum (Fig. S10b) have a binding energy of 495.0 eV (Sn $3d_{3/2}$) and 486.5 eV (Sn $3d_{5/2}$): the peak splitting of about 8.5 eV confirms the Sn^{+4} state as reported for CMTS [76,77]. Some residual SnS has been found close to the Mo layer: considering that Sn was the first metal deposited, it is possible that some binary sulphide was left unreacted on the bottom. The S 2p spectrum (Fig. S10c) is mostly composed of two contributions located at 162.5 eV (S $2p_{1/2}$) and 161.5 eV ($2p_{3/2}$): the peak splitting of about 1 eV confirms the S^{-2} state as reported for CMTS [76,77]; residual elemental S and Cu_2S has been detected in the upper layers [83,84], probably due to a non-uniform sulfurization of the metal stack.

Cu_2S was not detected by previous characterization techniques and the Cu2p high-resolution spectrum does not clearly show additional peaks [83,84], so it should be present in a small amount. But the most distressing detection comes from having found oxidized manganese in the bulk (mainly MnO_2 and some Mn_3O_4). Fig. 11b confirms the oxygen is present in all the TF, and it shows the Mn–O–Mn bond (529.7 eV), the Mn–O–H bond (531.8 eV), plus some water on the surface (H–O–H bond at 533.0 eV) [85]. XPS confirms that the HCl treatment removes most of the Mn_3O_4 from the surface but fails to remove the MnO_2. Due to the process requirements (avoiding Sn loss and Cu oxidation), Mn was deposited as the last metal in the stack, so it remains exposed to the atmosphere from when it comes out of the sputter deposition chamber to when it enters the sulfurization quartz tube. This air exposure causes Mn oxidation, which although partially cured by the annealing in the sulphur atmosphere, leaves impurities in the film. Mn_3O_4 is a wide band gap semiconductor (E_g ranging from 2.0 eV to 3.6 eV), mainly studied for sensors, memory, and energy storage devices [86,87], so it cannot be correlated to the D2 defect found by the PL analysis. On the other hand, MnO_2 has a narrow band gap: it is one of the most promising catalytic materials for environmental applications thanks to its earth-abundancy, low toxicity, low cost, high environmental compatibility, and acid resistance [88]. Unfortunately, the easy recombination of photo-generated electrons and holes, due to the extremely narrow bandgap, limits its application in photocatalysis [88]. The TT temperature is too low to promote the sulfurization of the oxide clusters, and the HCl cleaning is weakly effective on MnO_2. Assuming that the MnO_2 valence band under illumination is at the same level as the CMTS one [89], the MnO_2 conduction band should have the same energy of D2 detected by the PL analysis. If it was so, the low device performances could be ascribed to the presence of MnO_2 impurity, which acts as an easy path for charge recombination, wiping out the generated photo-current.

Admittance spectroscopy (AS) was implemented to reach a deeper understanding of the recombination mechanisms in the champion solar cell [90]. RT-AS measurements have been carried out to investigate the defects distribution after 15 months from the production time. The capacitance changes upon bias voltage (V_{bias}) and frequency (f) modulation: the variations can be plotted as loss maps (Fig. 12) to highlight nonlinear resistances and defects [90,91]. Fig. 12 compares the loss maps of the 15months aged **CMTS.02 + 50%**, **CMTS.02 + 50%+TT**, and **CMTS.02 + 50%+HCl + TT** devices.

CMTS.02 + 50% solar cell (Fig. 12a) shows the same features reported by Brammertz et al. [91] at low frequency for poorly performing solar cells, and correlated to high conduction through the p-n junction. The other two contributions in Fig. 12a at higher frequencies are quite like those reported for CZTS samples [90] and related to defects with high activation energies placed at the interface with CdS (vertical feature between 0 and 1 V), and at back contact barrier (horizontal feature at high frequency between −1.5 and 1 V). After TT and without the HCl etching (Fig. 12b), the contribution due to high conduction at the p-n junction is drastically reduced, meanwhile a wide new one appears in the centre of the loss map. Brammertz et al. [91] associated this feature with a bulk n-type defect. The defects at the CMTS/CdS are still present, but their attribution is less clear in Fig. 12b. The HCl treatment before the CdS deposition, combined with the TT on the entire device (Fig. 12c), furtherly clean the loss map. Defects located at the CMTS/CdS interface and in the bulk are still present, but the intensity is drastically reduced. Thus, HCl removes the CMTS secondary phases, while TT mainly improves the p-n junction. The defect at the centre of the loss maps of **CMTS.02 + 50%+TT** and **CMTS.02 + 50%+HCl + TT** (Fig. 12b–c) has been associated with CIGS-based solar cells with an

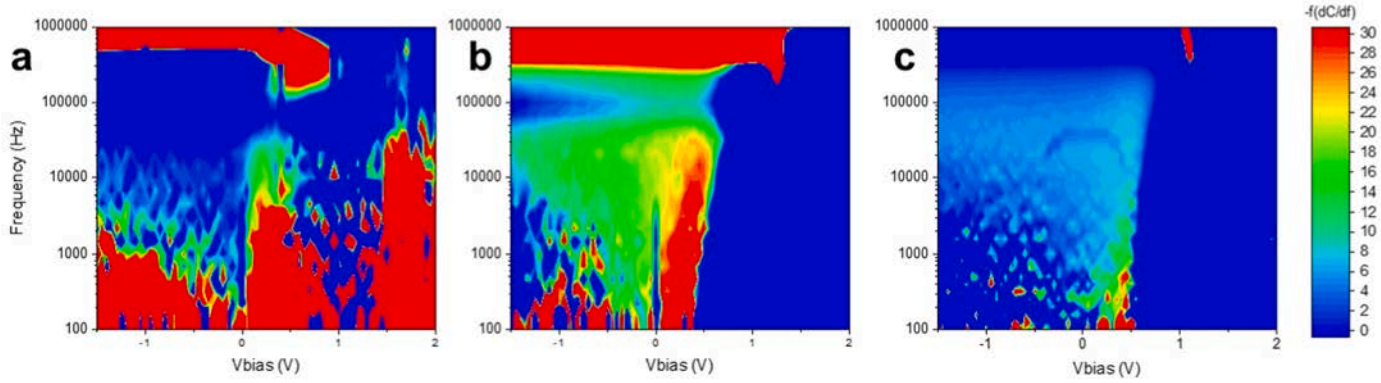

Fig. 12. Loss maps of (**a**) **CMTS.02 + 50%**, (**b**) **CMTS.02 + 50%+TT**, and (**c**) **CMTS.02 + 50%+HCl + TT** devices.

n-type deep defect [91]. Therefore, CMTS defectivity remains critical even after both PDTs. In particular, the antisite defects and MnO_2 recombine most of the photo-generated charge. Mn oxides could be drastically reduced by adopting wet methods for the CMTS synthesis: a precursor ink produced in an inert atmosphere could allow manganese control, as some of the authors made for the iron-substituted CZTS [92]. The antisite defects could be managed by employing rapid thermal processing to anneal the TF [93]. Finally, the CdS should be replaced both to obtain better PV performances than those obtained so far, but above all to produce truly environmentally friendly solar cells.

4. Conclusions

In conclusion, CMTS TFs per PV application have been sintered by a high-throughput two-step process (sputtering and sulfurization) and characterized to validate the CMTS potentialities to produce PV devices made by Earth-abundant light-absorbing layers. We investigated the correlation between the metals' ratio and the occurrence of main secondary phases: MnS in the alabandite structure and $Cu_2MnSn_3S_8$ in the thio-spinel structure. The Cu- and Mn-poor regime was identified as optimal to minimize the presence of secondary phases. Prototypal solar devices have been produced, and the implementation of post-deposition treatments investigated: an HCl etching was used to remove the residual binary sulphides, while a thermal treatment on the final device was employed to improve the p-n junction with the CdS. The delivered PV performances, ranging from 0.6% to 1.1%, were in line with the published literature. The reason for such a low value has a double nature with the same effect of bleaching the photo-generated charge: antisite defects and process residual MnO_2. Therefore, moving to deposition methods to be performed in a controlled environment, which does not foresee sulfurization processes, and the adoption of rapid thermal annealing is suggested to reduce the CMTS defectivity. These preliminary results pave the way to further works, pushing the research on promising manganese-based chalcogenides for PV applications. Moreover, fundamental research on CMTS and related PV devices should be focused on the design of a buffer layer to aid the increase of PV performance and even further reduce device toxicity.

CRediT authorship contribution statement

Vanira Trifiletti: Writing – review & editing, Writing – original draft, Visualization, Validation, Supervision, Software, Data curation. **Luigi Frioni:** Writing – original draft, Methodology, Investigation, Formal analysis, Data curation. **Giorgio Tseberlidis:** Writing – review & editing, Data curation. **Elisa Vitiello:** Writing – review & editing, Data curation. **Mati Danilson:** Data curation, Formal analysis, Investigation. **Maarja Grossberg:** Data curation, Methodology. **Maurizio Acciarri:** Formal analysis, Data curation. **Simona Binetti:** Writing – review & editing, Writing – original draft, Project administration, Funding acquisition. **Stefano Marchionna:** Writing – review & editing, Writing – original draft, Validation, Software, Project administration, Methodology, Investigation, Funding acquisition, Formal analysis, Data curation, Conceptualization.

Declaration of competing interest

The authors declare that they have no known competing financial interests or personal relationships that could have appeared to influence the work reported in this paper.

Data availability

Data will be made available on request.

Acknowledgement

This work was also supported by the project PON named "Bifacial Efficient Solar Cell Technology with 4-Terminal Architecture for Utility Scale" called "BEST-4U″, financed by the Italian Ministry for Universities and Research (MUR) (CUPB88D19000160005), and by the Ricerca Sistema Energetico (RSE S.p.A) under the Contract Agreement between RSE S.p.A. and the Ministry of Economic Development - General Directorate for the Electricity Market, Renewable Energy and Energy Efficiency, Nuclear Energy in compliance with the Decree of April 16th, 2018. The authors acknowledge the University of Milano-Bicocca through "Bando Infrastrutture di Ricerca 2021".

Appendix A. Supplementary data

Supplementary data to this article can be found online at https://doi.org/10.1016/j.solmat.2023.112247.

References

[1] M. Topic, R. Drozdowski, W. Sinke, G. Arrowsmith, A. Spoden, European Technology and Innovation Platform for Photovoltaics, *Strategic Research and Innovation Agenda on Photovoltaics*, 2022.
[2] NREL, The National Renewable Energy Laboratory, Best Research-Cell Efficiency Chart, 2022.
[3] M. Jamiati, An evaluation for CIGS based thin-film solar cells development, Journal of Interfaces, Thin Films, and Low dimensional systems 4 (2021) 365–378.
[4] S. Resalati, T. Okoroafor, A. Maalouf, E. Saucedo, M. Placidi, Life cycle assessment of different chalcogenide thin-film solar cells, Appl. Energy 313 (2022), 118888.
[5] R. Lee, H. Lee, D. Kim, J. Yoon, Performance evaluation of flexible CIGS modules based on operational data under outdoor conditions, Energy Sci. Eng. 10 (2022) 292–307.
[6] S. Giraldo, Z. Jehl, M. Placidi, V. Izquierdo-Roca, A. Pérez-Rodríguez, E. Saucedo, Progress and perspectives of thin film kesterite photovoltaic technology: a critical review, Adv. Mater. 31 (2019), 1806692.
[7] A. Le Donne, V. Trifiletti, S. Binetti, New earth-abundant thin film solar cells based on chalcogenides, 297, Front. Chem. 7 (2019) 297–309.

[8] M. He, C. Yan, J. Li, M.P. Suryawanshi, J. Kim, M.A. Green, X. Hao, Kesterite solar cells: insights into current strategies and challenges, Adv. Sci. 8 (2021), 2004313.
[9] E. Gervais, S. Shammugam, L. Friedrich, T. Schlegl, Raw material needs for the large-scale deployment of photovoltaics – effects of innovation-driven roadmaps on material constraints until 2050, Renew. Sustain. Energy Rev. 137 (2021), 110589.
[10] D. Sun, Y.-y. Ding, L.-w. Kong, L.-q. Wang, B.-x. Ding, Y.-h. Zhang, L.-m. Wei, L. Zhang, L.-x. Zhang, First principles calculation of the electronic-optical properties of Cu2MgSn(SxSe1−x)4, Optoelectron. Lett. 16 (2020) 29–33.
[11] J. Yu, H. Deng, Q. Zhang, J. Tao, L. Sun, P. Yang, J. Chu, The role of tuning Se/(S + Se) ratio in the improvement of Cu2MnSn(S, Se)4 thin films properties and photovoltaic device performance, Sol. Energy 179 (2019) 279–285.
[12] Y. Sun, X. Li, W. Qiao, L. Wu, S. Gao, H. Li, F. Liu, J. Ao, Y. Zhang, A promising photovoltaic material Cu2MnSn(S,Se)4: film growth and its application in solar cell, Sol. Energy Mater. Sol. Cell. 219 (2021), 110788.
[13] M.K. Nazeeruddin, A. Kay, I. Rodicio, R. Humphry-Baker, E. Mueller, P. Liska, N. Vlachopoulos, M. Graetzel, Conversion of light to electricity by cis-X2bis(2,2'-bipyridyl-4,4'-dicarboxylate)ruthenium(II) charge-transfer sensitizers (X = Cl-, Br-, I-, CN-, and SCN-) on nanocrystalline titanium dioxide electrodes, J. Am. Chem. Soc. 115 (1993) 6382–6390.
[14] X. Li, Z. Hou, S. Gao, Y. Zeng, J. Ao, Z. Zhou, B. Da, W. Liu, Y. Sun, Y. Zhang, Efficient optimization of the performance of Mn2+-doped kesterite solar cell: machine learning aided synthesis of high efficient Cu2(Mn,Zn)Sn(S,Se)4 solar cells, Solar RRL 2 (2018), 1800198.
[15] K. Pal, P. Singh, A. Bhaduri, K.B. Thapa, Current challenges and future prospects for a highly efficient (>20%) kesterite CZTS solar cell: a review, Sol. Energy Mater. Sol. Cell. 196 (2019) 138–156.
[16] T. Pansuriya, R. Malani, V. Kheraj, Investigations on the effect of buffer layer on CMTS based thin film solar cell using SCAPS 1-D, Opt. Mater. 126 (2022), 112150.
[17] Y. Cui, R. Deng, G. Wang, D. Pan, A general strategy for synthesis of quaternary semiconductor Cu2MSnS4 (M = Co2+, Fe2+, Ni2+, Mn2+) nanocrystals, J. Mater. Chem. 22 (2012) 23136–23140.
[18] H. Guan, H. Hou, M. Li, J. Cui, Photocatalytic and thermoelectric properties of Cu2MnSnS4 nanoparticles synthesized via solvothermal method, Mater. Lett. 188 (2017) 319–322.
[19] Y. Xie, C. Zhang, G. Yang, J. Yang, X. Zhou, J. Ma, Highly crystalline stannite-phase Cu2XSnS4 (X = Mn, Fe, Co, Ni, Zn and Cd) nanoflower counter electrodes for ZnO-based dye-sensitised solar cells, J. Alloys Compd. 696 (2017) 938–946.
[20] X. Liang, P. Guo, G. Wang, R. Deng, D. Pan, X. Wei, Dilute magnetic semiconductor Cu2MnSnS4 nanocrystals with a novel zincblende and wurtzite structure, RSC Adv. 2 (2012) 5044–5046.
[21] A. Sarilmaz, F. Ozel, A. Karabulut, İ. Orak, M.A. Şahinkaya, The effects of temperature and frequency changes on the electrical characteristics of hot-injected Cu2MnSnS4 chalcogenide-based heterojunction, Phys. B Condens. Matter 580 (2020), 411821.
[22] L. Chen, H. Deng, J. Tao, H. Cao, L. Huang, L. Sun, P. Yang, J. Chu, Synthesis and characterization of earth-abundant Cu2MnSnS4 thin films using a non-toxic solution-based technique, RSC Adv. 5 (2015) 84295–84302.
[23] S. Lie, W. Li, S.W. Leow, D.M. Bishop, O. Gunawan, L. Helena Wong, Comparing the effect of Mn substitution in sulfide and sulfoselenide-based kesterite solar cells, Solar RRL 4 (2020), 1900521.
[24] L. Chen, H. Deng, J. Tao, W. Zhou, L. Sun, F. Yue, P. Yang, J. Chu, Influence of annealing temperature on structural and optical properties of Cu2MnSnS4 thin films fabricated by sol–gel technique, J. Alloys Compd. 640 (2015) 23–28.
[25] L.L. Chen, H.M. Deng, K.Z. Zhang, L. Huang, J. Liu, L. Sun, P.X. Yang, J.H. Chu, Structural and Optical Properties of Cu2MnSnS4 Thin Film Fabricated by Sol-Gel Technique, 39, 2015, pp. 39–43.
[26] S. Lie, M.I. Sandi, Y.F. Tay, W. Li, J.M.R. Tan, D.M. Bishop, O. Gunawan, L. H. Wong, Improving the charge separation and collection at the buffer/absorber interface by double-layered Mn-substituted CZTS, Sol. Energy Mater. Sol. Cell. 185 (2018) 351–358.
[27] S. Podsiadlo, M. Bialoglowski, M. Fadaghi, W. Gebicki, C. Jastrzebski, E. Zero, D. Trzybinski, K. Wozniak, Synthesis of magnetic doped kesterite single crystals, Cryst. Res. Technol. 50 (2015) 690–694.
[28] X. Wang, T. Liu, H. Guan, F. Yu, H. Hou, A comparative study of cu2mnsns4 thin films synthesized via different chemical methods, Optoelectronics and Advanced Materials, Rapid Communications 9 (2015) 1190–1193.
[29] A. Ziti, B. Hartiti, A. Belafhaili, H. Labrim, S. Fadili, A. Ridah, M. Tahri, P. Thevenin, Growth and characterization of pure stannite Cu2MnSnS4 thin films deposited by dip-coating technique, Appl. Phys. A 127 (2021) 663.
[30] R.R. Prabhakar, S. Zhenghua, Z. Xin, T. Baikie, L.S. Woei, S. Shukla, S.K. Batabyal, O. Gunawan, L.H. Wong, Photovoltaic effect in earth abundant solution processed Cu2MnSnS4 and Cu2MnSn(S,Se)4 thin films, Sol. Energy Mater. Sol. Cell. 157 (2016) 867–873.
[31] I.G. Orletskii, P.D. Mar'yanchuk, M.N. Solovan, E.V. Maistruk, D.P. Kozyarskii, Electrical and optical properties of Cu2Zn(Fe,Mn)SnS4 films prepared by spray pyrolysis, Tech. Phys. 63 (2018) 243–249.
[32] S. Dridi, E. Aubry, N. Bitri, F. Chaabouni, P. Briois, Growth and characterization of Cu2MnSnS4 thin films synthesized by spray pyrolysis under air atmosphere, Coatings 10 (2020) 963.
[33] A.S. Hassanien, I.M. El Radaf, Optical characterizations of quaternary Cu2MnSnS4 thin films: novel synthesis process of film samples by spray pyrolysis technique, Phys. B Condens. Matter 585 (2020), 412110.
[34] S. Marchionna, A. Le Donne, M. Merlini, S. Binetti, M. Acciarri, F. Cernuschi, Growth of Cu2MnSnS4 PV absorbers by sulfurization of evaporated precursors, J. Alloys Compd. 693 (2017) 95–102.
[35] K. Rudisch, W.F. Espinosa-García, J.M. Osorio-Guillén, C.M. Araujo, C. Platzer-Björkman, J.J.S. Scragg, Structural and electronic properties of Cu2MnSnS4 from experiment and first-principles calculations, Phys. Status Solidi 256 (2019), 1800743.
[36] J. Yu, H. Deng, J. Tao, L. Chen, H. Cao, L. Sun, P. Yang, J. Chu, Synthesis of Cu2MnSnS4 thin film deposited on seeded fluorine doped tin oxide substrate via a green and low-cost electrodeposition method, Mater. Lett. 191 (2017) 186–188.
[37] J. Yu, H. Deng, L. Chen, J. Tao, Q. Zhang, B. Guo, L. Sun, P. Yang, X. Zheng, J. Chu, Improvement performance of two-step electrodepositing Cu2MnSnS4 thin film solar cells by tuning Cu-Sn alloy layer deposition time, Mater. Chem. Phys. 211 (2018) 382–388.
[38] J.H. Malik, M.B. Zaman, R. Poolla, K.A. Malik, I. Assadullah, A.A. Bhat, R. Tomar, Hydrothermal synthesis of tetragonal and wurtzite Cu2MnSnS4 nanostructures for multiple applications: influence of different sulfur reactants on growth and properties, Mater. Sci. Semicond. Process. 121 (2021), 105438.
[39] E. Waluś, M. Manecki, G. Cios, T. Tokarski, Effect of a sulfur precursor on the hydrothermal synthesis of Cu2MnSnS4, Materials 14 (2021) 3457.
[40] A. Le Donne, S. Marchionna, M. Acciarri, F. Cernuschi, S. Binetti, Relevant efficiency enhancement of emerging Cu2MnSnS4 thin film solar cells by low temperature annealing, Sol. Energy 149 (2017) 125–131.
[41] S. Marchionna, P. Garattini, A. Le Donne, M. Acciarri, S. Tombolato, S. Binetti, Cu2ZnSnS4 solar cells grown by sulphurisation of sputtered metal precursors, Thin Solid Films 542 (2013) 114–118.
[42] J. Tauc, R. Grigorovici, A. Vancu, Optical properties and electronic structure of amorphous germanium, Phys. Status Solidi 15 (1966) 627–637.
[43] A. Le Donne, S. Marchionna, P. Garattini, R.A. Mereu, M. Acciarri, S. Binetti, Effects of CdS buffer layers on photoluminescence properties of Cu2ZnSnS4 solar cells, 2015, Int. J. Photoenergy (2015) 8.
[44] G. Tseberlidis, A. Hasan Husien, S. Riva, L. Frioni, A. Le Donne, M. Acciarri, S. Binetti, Semi-transparent Cu2ZnSnS4 solar cells by drop-casting of sol-gel ink, Sol. Energy 224 (2021) 134–141.
[45] G. Tseberlidis, V. Trifiletti, A. Le Donne, L. Frioni, M. Acciarri, S. Binetti, Kesterite solar-cells by drop-casting of inorganic sol–gel inks, Sol. Energy 208 (2020) 532–538.
[46] H. Katagiri, K. Jimbo, M. Tahara, H. Araki, K. Oishi, The influence of the composition ratio on CZTS-based thin film solar cells, MRS Proceedings 1165 (2011), 1165-M1104-1101.
[47] D. Han, Y.Y. Sun, J. Bang, Y.Y. Zhang, H.-B. Sun, X.-B. Li, S.B. Zhang, Deep electron traps and origin of p-type conductivity in the earth-abundant solar-cell material Cu_2ZnSnS_4, Phys. Rev. B 87 (2013), 155206.
[48] T. Shibuya, Y. Goto, Y. Kamihara, M. Matoba, K. Yasuoka, L.A. Burton, A. Walsh, From kesterite to stannite photovoltaics: stability and band gaps of the Cu2(Zn,Fe)SnS4 alloy, Appl. Phys. Lett. 104 (2014), 021912.
[49] W. Li, J. Chen, C. Yan, X. Hao, The effect of ZnS segregation on Zn-rich CZTS thin film solar cells, J. Alloys Compd. 632 (2015) 178–184.
[50] A.D. Smigelskas, Zinc Diffusion in Alpha Brass, 1947.
[51] S. Harada, Some new sulfo-spinels containing iron-group transition metals, Mater. Res. Bull. 8 (1973) 1361–1369.
[52] P.A. Fernandes, P.M.P. Salomé, A.F. da Cunha, Study of polycrystalline Cu2ZnSnS4 films by Raman scattering, J. Alloys Compd. 509 (2011) 7600–7606.
[53] A. Gueddim, N. Bouarissa, A. Naas, F. Daoudi, N. Messikine, Characteristics and optimization of ZnO/CdS/CZTS photovoltaicsolar cell, Appl. Phys. A 124 (2018) 199.
[54] G. Refantero, E.C. Prima, A. Setiawan, C. Panatarani, D. Cahyadi, B. Yuliarto, Etching process optimization of non-vacuum fabricated Cu2ZnSnS4 solar cell, J. Mater. Sci. Mater. Electron. 31 (2020) 3674–3680.
[55] M.F. Sanchez, T.G. Sanchez, M. Courel, O. Reyes-Vallejo, Y. Sanchez, E. Saucedo, P. J. Sebastian, Effect of post annealing thermal heating on Cu2ZnSnS4 solar cells processed by sputtering technique, Sol. Energy 237 (2022) 196–202.
[56] G. Tseberlidis, V. Di Palma, V. Trifiletti, L. Frioni, M. Valentini, C. Malerba, A. Mittiga, M. Acciarri, S.O. Binetti, Titania as buffer layer for Cd-free kesterite solar cells, ACS Materials Letters (2022) 219–224.
[57] M. Neuschitzer, Y. Sanchez, T. Olar, T. Thersleff, S. Lopez-Marino, F. Oliva, M. Espindola-Rodriguez, H. Xie, M. Placidi, V. Izquierdo-Roca, I. Lauermann, K. Leifer, A. Pérez-Rodriguez, E. Saucedo, Complex surface chemistry of kesterites: Cu/Zn reordering after low temperature postdeposition annealing and its role in high performance devices, Chem. Mater. 27 (2015) 5279–5287.
[58] W.-C. Chen, C.-Y. Chen, Y.-R. Lin, J.-K. Chang, C.-H. Chen, Y.-P. Chiu, C.-I. Wu, K.-H. Chen, L.-C. Chen, Interface engineering of CdS/CZTSSe heterojunctions for enhancing the Cu2ZnSn(S,Se)4 solar cell efficiency, Mater. Today Energy 13 (2019) 256–266.
[59] C. Yan, J. Huang, K. Sun, S. Johnston, Y. Zhang, H. Sun, A. Pu, M. He, F. Liu, K. Eder, L. Yang, J.M. Cairney, N.J. Ekins-Daukes, Z. Hameiri, J.A. Stride, S. Chen, M.A. Green, X. Hao, Cu2ZnSnS4 solar cells with over 10% power conversion efficiency enabled by heterojunction heat treatment, Nat. Energy 3 (2018) 764–772.
[60] L. Sanghyun, J.P. Kent, Spectral responses in quantum efficiency of emerging kesterite thin-film solar cells, Rijeka, in: L.P. Sergei, B. John (Eds.), Optoelectronics, IntechOpen, 2017. Ch. 16.
[61] D.-I. Kim, C.-W. Jeon, Aging effect on the efficiency of Cu(In,Ga)Se2/CdS solar cells, Electron. Mater. Lett. 11 (2015) 1048–1052.
[62] T. Ott, F. Schönberger, T. Walter, D. Hariskos, O. Kiowski, R. Schäffler, Long Term Endurance Test and Contact Degradation of CIGS Solar Cells, SPIE, 2013.
[63] V.D. Trifiletti T, N. Manfredi, O. Fenwick, S Rizzo Colella, Molecular doping for hole transporting materials in hybrid perovskite solar cells, Metals 10 (2020).

[64] The physics of the solar cell, in: Handbook of Photovoltaic Science and Engineering, pp. 82-129.
[65] J. Krustok, H. Collan, K. Hjelt, Does the low-temperature Arrhenius plot of the photoluminescence intensity in CdTe point towards an erroneous activation energy? J. Appl. Phys. 81 (1997) 1442–1445.
[66] S. Oueslati, M. Grossberg, M. Kauk-Kuusik, V. Mikli, K. Ernits, D. Meissner, J. Krustok, Effect of germanium incorporation on the properties of kesterite Cu2ZnSn(S,Se)4 monograins, Thin Solid Films 669 (2019) 315–320.
[67] J. Krustok, T. Raadik, M. Grossberg, M. Kauk-Kuusik, V. Trifiletti, S. Binetti, Photoluminescence study of deep donor- deep acceptor pairs in Cu2ZnSnS4, Mater. Sci. Semicond. Process. 80 (2018) 52–55.
[68] M. Grossberg, T. Raadik, J. Raudoja, J. Krustok, Photoluminescence study of defect clusters in Cu2ZnSnS4 polycrystals, Curr. Appl. Phys. 14 (2014) 447–450.
[69] S. Oueslati, G. Brammertz, M. Buffière, C. Köble, T. Oualid, M. Meuris, J. Poortmans, Photoluminescence study and observation of unusual optical transitions in Cu2ZnSnSe4/CdS/ZnO solar cells, Sol. Energy Mater. Sol. Cell. 134 (2015) 340–345.
[70] M. Sahu, V.R. Minnam Reddy, C. Park, P. Sharma, Review article on the lattice defect and interface loss mechanisms in kesterite materials and their impact on solar cell performance, Sol. Energy 230 (2021) 13–58.
[71] J.J.S. Scragg, L. Choubrac, A. Lafond, T. Ericson, C. Platzer-Björkman, A low-temperature order-disorder transition in Cu2ZnSnS4 thin films, Appl. Phys. Lett. 104 (2014), 041911.
[72] J.J.S. Scragg, J.K. Larsen, M. Kumar, C. Persson, J. Sendler, S. Siebentritt, C. Platzer Björkman, Cu–Zn disorder and band gap fluctuations in Cu2ZnSn(S,Se)4: theoretical and experimental investigations, Phys. Status Solidi 253 (2016) 247–254.
[73] Z.-K. Yuan, S. Chen, H. Xiang, X.-G. Gong, A. Walsh, J.-S. Park, I. Repins, S.-H. Wei, Engineering solar cell absorbers by exploring the band alignment and defect disparity: the case of Cu- and Ag-based kesterite compounds, Adv. Funct. Mater. 25 (2015) 6733–6743.
[74] K. Timmo, M. Altosaar, M. Pilvet, V. Mikli, M. Grossberg, M. Danilson, T. Raadik, R. Josepson, J. Krustok, M. Kauk-Kuusik, The effect of Ag alloying of Cu2(Zn,Cd)SnS4 on the monograin powder properties and solar cell performance, J. Mater. Chem. 7 (2019) 24281–24291.
[75] R. Chen, C. Persson, Electronic and optical properties of Cu2XSnS4 (X = Be, Mg, Ca, Mn, Fe, and Ni) and the impact of native defect pairs, J. Appl. Phys. 121 (2017), 203104.
[76] L. Chen, H. Deng, J. Tao, H. Cao, L. Sun, P. Yang, J. Chu, Strategic improvement of Cu2MnSnS4 films by two distinct post-annealing processes for constructing thin film solar cells, Acta Mater. 109 (2016) 1–7.
[77] L. Nie, J. Yang, D. Yang, S. Liu, Effect of substrate temperature on growth and properties of Cu2MnSnS4 thin films prepared by chemical spray pyrolysis, J. Mater. Sci. Mater. Electron. 30 (2019) 3760–3766.
[78] S. Lie, J.M. Rui Tan, W. Li, S.W. Leow, Y.F. Tay, D.M. Bishop, O. Gunawan, L. H. Wong, Reducing the interfacial defect density of CZTSSe solar cells by Mn substitution, J. Mater. Chem. 6 (2018) 1540–1550.
[79] M.B. Zakaria, C. Li, M. Pramanik, Y. Tsujimoto, M. Hu, V. Malgras, S. Tominaka, Y. Yamauchi, Nanoporous Mn-based electrocatalysts through thermal conversion of cyano-bridged coordination polymers toward ultra-high efficiency hydrogen peroxide production, J. Mater. Chem. 4 (2016) 9266–9274.
[80] X. Zheng, L. Yu, B. Lan, G. Cheng, T. Lin, B. He, W. Ye, M. Sun, F. Ye, Three-dimensional radial α-MnO2 synthesized from different redox potential for bifunctional oxygen electrocatalytic activities, J. Power Sources 362 (2017) 332–341.
[81] R.A. Davoglio, G. Cabello, J.F. Marco, S.R. Biaggio, Synthesis and characterization of α-MnO2 nanoneedles for electrochemical supercapacitors, Electrochim. Acta 261 (2018) 428–435.
[82] E.S. Ilton, J.E. Post, P.J. Heaney, F.T. Ling, S.N. Kerisit, XPS determination of Mn oxidation states in Mn (hydr)oxides, Appl. Surf. Sci. 366 (2016) 475–485.
[83] Y. Xie, A. Riedinger, M. Prato, A. Casu, A. Genovese, P. Guardia, S. Sottini, C. Sangregorio, K. Miszta, S. Ghosh, T. Pellegrino, L. Manna, Copper sulfide nanocrystals with tunable composition by reduction of covellite nanocrystals with Cu+ ions, J. Am. Chem. Soc. 135 (2013) 17630–17637.
[84] M. Kundu, T. Hasegawa, K. Terabe, M. Aono, Effect of sulfurization conditions on structural and electrical properties of copper sulfide films, J. Appl. Phys. 103 (2008), 073523.
[85] G. Xie, X. Liu, Q. Li, H. Lin, Y. Li, M. Nie, L. Qin, The evolution of α-MnO2 from hollow cubes to hollow spheres and their electrochemical performance for supercapacitors, J. Mater. Sci. 52 (2017) 10915–10926.
[86] N.M. Hosny, A. Dahshan, Facile synthesis and optical band gap calculation of Mn3O4 nanoparticles, Mater. Chem. Phys. 137 (2012) 637–643.
[87] V. Pandey Adiba, S. Munjal, T. Ahmad, Optical properties and spectroscopic investigation of single phase tetragonal Mn3O4 nanoparticles, Mater. Today Proc. 26 (2020) 1181–1183.
[88] R. Yang, Y. Fan, R. Ye, Y. Tang, X. Cao, Z. Yin, Z. Zeng, MnO2-Based materials for environmental applications, Adv. Mater. 33 (2021), 2004862.
[89] B.A. Pinaud, Z. Chen, D.N. Abram, T.F. Jaramillo, Thin films of sodium birnessite-type MnO2: optical properties, electronic band structure, and solar photoelectrochemistry, J. Phys. Chem. C 115 (2011) 11830–11838.
[90] M. Kauk-Kuusik, K. Timmo, K. Muska, M. Pilvet, J. Krustok, R. Josepson, G. Brammertz, B. Vermang, M. Danilson, M. Grossberg, Detailed insight into the CZTS/CdS interface modification by air annealing in monograin layer solar cells, ACS Appl. Energy Mater. 4 (2021) 12374–12382.
[91] G. Brammertz, T. Kohl, J.d. Wild, D.G. Buldu, G. Birant, M. Meuris, J. Poortmans, B. Vermang, Bias-dependent admittance spectroscopy of thin-film solar cells: experiment and simulation, IEEE J. Photovoltaics 10 (2020) 1102–1111.
[92] V. Trifiletti, G. Tseberlidis, M. Colombo, A. Spinardi, S. Luong, M. Danilson, M. Grossberg, O. Fenwick, S. Binetti, Growth and characterization of Cu2Zn1−xFexSnS4 thin films for photovoltaic applications, Materials 13 (2020) 1471.
[93] M. Kumar, A. Dubey, N. Adhikari, S. Venkatesan, Q. Qiao, Strategic review of secondary phases, defects and defect-complexes in kesterite CZTS-Se solar cells, Energy Environ. Sci. 8 (2015) 3134–3159.